Neuroscience 595 (2026) 59–72

Contents lists available at ScienceDirect

Neuroscience

journal homepage: www.elsevier.com/locate/nsc

Research Article

Non-canonical role of DNA mismatch repair on sensory processing in mice

Sadia N. Rahman [a,e,1], Demetrios Neophytou [b], Siboney Oviedo-Gray [c], Bao Q. Vuong [d], Hysell V. Oviedo [c,*]

[a] *Department of Biology, The City College of New York, NY, USA*
[b] *Neuroscience, City University of New York Graduate Center, New York, NY, USA*
[c] *Washington University School of Medicine, Department of Neuroscience, St. Louis, MO, USA*
[d] *Biology, Graduate Center, Department of Biology, The City College of New, The City University of New York, NY, USA*
[e] *Department of Biology, The City College of New York, The City University of New York, NY, USA*

ARTICLE INFO

Keywords:
DNA repair
Sensory deficits
Genotoxicity
Parvalbumin interneurons
Thalamic Reticular Nucleus

ABSTRACT

DNA repair mechanisms are essential for cellular development and function. In post-mitotic neurons, deficiencies in DNA damage response proteins can lead to severe neurodegenerative and neurodevelopmental disorders. One highly conserved factor involved in DNA repair is MutS Homolog 2 (*Msh2*), which is responsible for correcting base–base mismatches and insertion/deletion loops during cell proliferation. However, its role in mature neurons remains poorly understood. This study investigates the impact of *Msh2* loss on sensory processing in mice. Using electrophysiological and molecular assays, we identified significant deficits in cortical and thalamic sound processing in *Msh2*$^{-/-}$ mice. These deficits were linked to dysfunction of the thalamic reticular nucleus (TRN), which critically regulates corticothalamic and thalamocortical activity. Our findings revealed increased oxidative damage, aberrant neuronal activity, and elevated parvalbumin (PV) expression in PV^{+} neurons in the TRN of *Msh2*$^{-/-}$ mice. Additionally, we observed the presence of connexin plaques, indicating that disrupted gap junction formation may contribute to impaired TRN function. These results highlight *Msh2*'s crucial role in supporting PV^{+} neurons in the TRN, profoundly influencing sensory processing. This study provides new insight into how DNA repair mechanisms regulate neuronal development and function in a region-specific manner, potentially contributing to our understanding of their role in neurological disorders.

Introduction

A critical function of cells is their ability to recognize and repair genotoxicity over the course of a cell's lifetime, as it may accumulate close to 10^5 lesions per day (Hoeijmakers, 2009). This is especially crucial in the context of post-mitotic cells, such as neurons. In these cells, the abrogation of different proteins involved in the DNA damage response often leads to a wide range of severe neurodegenerative and neurodevelopmental disorders, such as xeroderma pigmentosum, Cockayne syndrome, and ataxia telangiectasia (McKinnon, 2009). The critical role of DNA repair pathways in maintaining genome integrity and their importance in the development and maintenance of the nervous system underscore their significance in preventing neurological disorders (McKinnon, 2009; Orii et al., 2006). One highly conserved repair pathway, mismatch repair (MMR), is used by cells to target base–base mismatches and insertion-deletion loops (IDLs) (Liu et al., 2017). Monoallelic deficiencies in any of the MutS homolog proteins (MSH2, MSH3, or MSH6) can result in microsatellite instability, while biallelic mutations in MMR factors (known as constitutional mismatch repair deficiency syndrome) are characterized by agenesis of the corpus callosum (CC), a tendency to form aggressive glioblastomas, and increased oxidized DNA (Jiricny, 2006; Tamura, 2019; Baas, 2013; Aronson, 2022; Russo, 2009). Recent studies also show MMR's influence in trinucleotide repeat expansion diseases such as Huntington's disease, myotonic dystrophy, and fragile X syndrome. However, the mechanisms by which MMR contributes to these diseases and syndromes are unknown (Iyer et al., 2015; Kovalenko, 2012; Schmidt and Pearson, 2016). Moreover, whether or how MMR plays a role in the function of terminally differentiated cells (e.g. post-mitotic neurons) has not been established (Fishel et al., 2007; Iyama and Wilson, 2013), and this study aims to investigate this question. Unraveling the role of MMR in neural function has the potential to reveal mechanisms underlying

---

* Corresponding author.
E-mail address: hysell@wustl.edu (H.V. Oviedo).
[1] Current address.

https://doi.org/10.1016/j.neuroscience.2025.12.066
Received 3 July 2025; Accepted 27 December 2025

neurodegenerative disorders, brain development, and the overall maintenance of neuronal health.

An essential component for the assembly of various recruitment complexes that target sites of mismatch is MSH2 (MutS homolog 2), which heterodimerizes with MSH3 and MSH6 to repair DNA (Tamura, 2019). *In-situ* hybridization data shows that *Msh2* is ubiquitously expressed across different brain regions, including the hippocampus, cortex, thalamus, and hypothalamus (Allen Brain Atlas). Broadly expressed genes are more likely to be involved in core functions required for cellular homeostasis, including DNA repair, general transcription, and metabolic regulation (Ramskold et al., 2009). In one of the few studies examining the impact of *Msh2* deficiency on brain function, a notable association was observed with dysmyelination of axonal projections in the corpus callosum of mice (Diouf, 2016). Nevertheless, MMR is expected to play an important role in glial cells, such as oligodendrocytes, due to their capacity for proliferation, which aligns with MMR's well-conserved function in DNA replication. Therefore, MMR's specific involvement and impact on non-proliferative cells, such as neurons, are not yet well understood.

In this study, we employed a top-down approach to examine the effects of *Msh2* deficiency on neuronal function. Deficits arising from neurogenetic disorders can present as weak or noisy processing deficits in ascending neural pathways, gradually accumulating and leading to significant high-level dysfunction (Robertson, 2014). We screened for auditory processing deficits in adult *Msh2*$^{-/-}$ mice (de Wind et al., 1995) using a combination of electrophysiological and molecular assays. We observed a widespread decrease in sound-evoked activity in the auditory cortex (ACx) of *Msh2*$^{-/-}$ mice, and hypothesized dysfunction in subcortical regions that play a critical role in modulating cortical and thalamic activity. Specifically, we implicate thalamic reticular nucleus (TRN) pathology as a possible cause of sensory processing deficits in *Msh2*$^{-/-}$ mice. Molecular assays revealed that abnormal cellular function and oxidative damage were significantly enhanced in the TRN, and electrophysiological recordings uncovered aberrant patterns of neural activity. Altogether, these data suggest that *Msh2*, and therefore MMR, play an important role in the development or maintenance of the TRN, thereby supporting downstream cortical processing.

Results

Thalamo-cortical loss of sound processing function in Msh2-null mice

We stained for the protein product of the immediate early gene *c-Fos* to detect recently active neurons and screened multiple brain regions in both *Msh2*$^{+/+}$ and *Msh2*$^{-/-}$ mice. We observed heterogeneous, brain-wide differences in neural activity between genotypes. For example, hippocampal activity was comparable across groups, whereas *c-Fos* expression in the somatosensory cortex and frontal lobes was significantly reduced in *Msh2*$^{-/-}$ mice (Fig. 1a, b). Additional examples of region-specific differences will be presented throughout the paper. To begin exploring the etiology of mechanisms underlying reduced cortical activity, we focused on sensory processing deficits in the auditory system. Sensory processing depends on the coordinated function of cellular and circuit-level mechanisms. Considering the potential role of MMR in neuronal function and development, we postulated that the loss of *Msh2* could initiate a cascade of neuronal dysfunction, in a way that particularly impairs higher-order brain regions like the auditory cortex (Robertson, 2014).

Changes in sensory input cause an increase in neuronal activity, which can lead to elevated expression of immediate early genes. To screen for changes in sound-evoked responses as a result of *Msh2* loss, we presented auditory stimuli (Fig. 1c) to evoke neuronal activity in the ACx and quantified *c-Fos*$^{+}$ neurons. Using frequency sweeps, we stimulated *Msh2*$^{+/+}$ mice and observed the previously reported lateralized activity, indicated by the increased number of c-Fos^{+} cells in layers 2/3 (L2/3) of the right ACx compared to the left ACx (Levy, 2019) (Fig. 1d (i, ii)). In the absence of *Msh2*, however, a significant decrease in *c-Fos*$^{+}$ neurons was observed in both auditory cortices, and lateralized activation of the auditory cortices was also abolished (Fig. 1d (iii, iv) and 1e). These results suggest that the loss of *Msh2* leads to significant hypoactivity and impairment in normal sensory processing functions within the ACx.

To examine in greater detail the extent of sound processing deficits in the ACx of *Msh2*$^{-/-}$ mice, we recorded multiunit neural activity using silicon probes that spanned L2-L6 (Fig. 2a). Multiunit responses were sorted using Kilosort (see Methods) to identify clusters of spikes from putative single units. Interestingly, we observed tone-evoked firing in *Msh2*$^{-/-}$ animals, albeit significantly lower than in *Msh2*$^{+/+}$ (Fig. 2b-c). We examined differences in frequency encoding between the genotypes by analyzing the tone-responsive fields of single units. We found a significant disparity in intensity thresholds between the two genotypes (Fig. 2d). This finding indicates a considerable increase in the sound level intensity required to elicit sound-evoked responses in *Msh2*$^{-/-}$ mice. In addition, we examined potential differences in the frequency response bandwidth. This metric captures the span of frequencies over which there is a measurable response above threshold. We performed this analysis at 50 dB and 80 dB (termed BW30 and BW60) in clusters of both genotypes (Fig. 2e). While there were no significant differences at BW60, the BW30 was significantly narrower in *Msh2*$^{-/-}$ (1.48 octaves) compared to *Msh2*$^{+/+}$ clusters (2.29 octaves). Because we observed reduced basal *c-Fos* expression in non-auditory cortical regions (Fig. 1a), we next asked whether spontaneous activity was similarly reduced in the ACx. Consistent with this prediction, spontaneous spiking activity during unstimulated trials also showed significantly lower firing rates in *Msh2*$^{-/-}$ compared to *Msh2*$^{+/+}$ (Fig. 2f). Together, these results suggest reduced basal activity and dynamic range in encoding frequency information, compromising the network's ability to respond to simple and complex sounds. The *c-Fos* data and direct recordings of neural activity reveal significant and widespread deficits in sensory-evoked activity in the ACx of *Msh2*$^{-/-}$ mice and point to possible dysfunction in subcortical processing stations.

To screen for sound processing deficits in subcortical auditory areas, we examined *c-Fos* expression in the ventral division of the geniculate nucleus (MGBv). This analysis was performed in the same animals stimulated with frequency sweeps and quantified for *c-Fos* expression in the ACx (Fig. 1). The MGBv is an obligatory relay for all ascending auditory information, ultimately projecting to the ACx. We found that *Msh2*$^{-/-}$ animals had a significant decrease in *c-Fos*$^{+}$ neurons in the MGBv compared to their *Msh2*$^{+/+}$ littermates, suggesting decreased neural activity in ascending auditory pathways (Fig. 3a-b). Interestingly, the number of *c-Fos*$^{+}$ neurons in the inferior colliculus (IC), an area that provides auditory input to the MGBv (Peruzzi et al., 1997), was not significantly different between *Msh2*$^{-/-}$ and *Msh2*$^{+/+}$ animals (Supplementary Fig. 1). Based on this evidence, we reasoned that the sensory processing deficits we see in *Msh2*$^{-/-}$ ACx could arise from intra-thalamic processing.

Thalamic reticular nucleus dysfunction in Msh2$^{-/-}$ *mice*

We asked whether deficits in thalamocortical (TC) activity could result from dysfunction of the thalamic reticular nucleus. The TRN, a shell of largely GABAergic inhibitory neurons in the dorsal thalamus, gates the bidirectional flow of information between the primary and secondary cortices and first- and higher-order projection neurons (Crabtree, 2018). TRN neurons receive glutamatergic inputs from the thalamus and send GABAergic efferents to TC projection neurons, partaking in feedforward and feedback inhibitory circuits involving the sensory cortices and thalamus (Fig. 3c). We examined *c-Fos* expression in the TRN of sweep stimulated animals and found a significant increase in *c-Fos*$^{+}$ neurons in *Msh2*$^{-/-}$ compared to *Msh2*$^{+/+}$ (Fig. 3d-e). These results support our findings of reduced sound-evoked *c-Fos* expression in the MGBv of *Msh2*$^{-/-}$: since the output of the TRN is inhibitory, higher

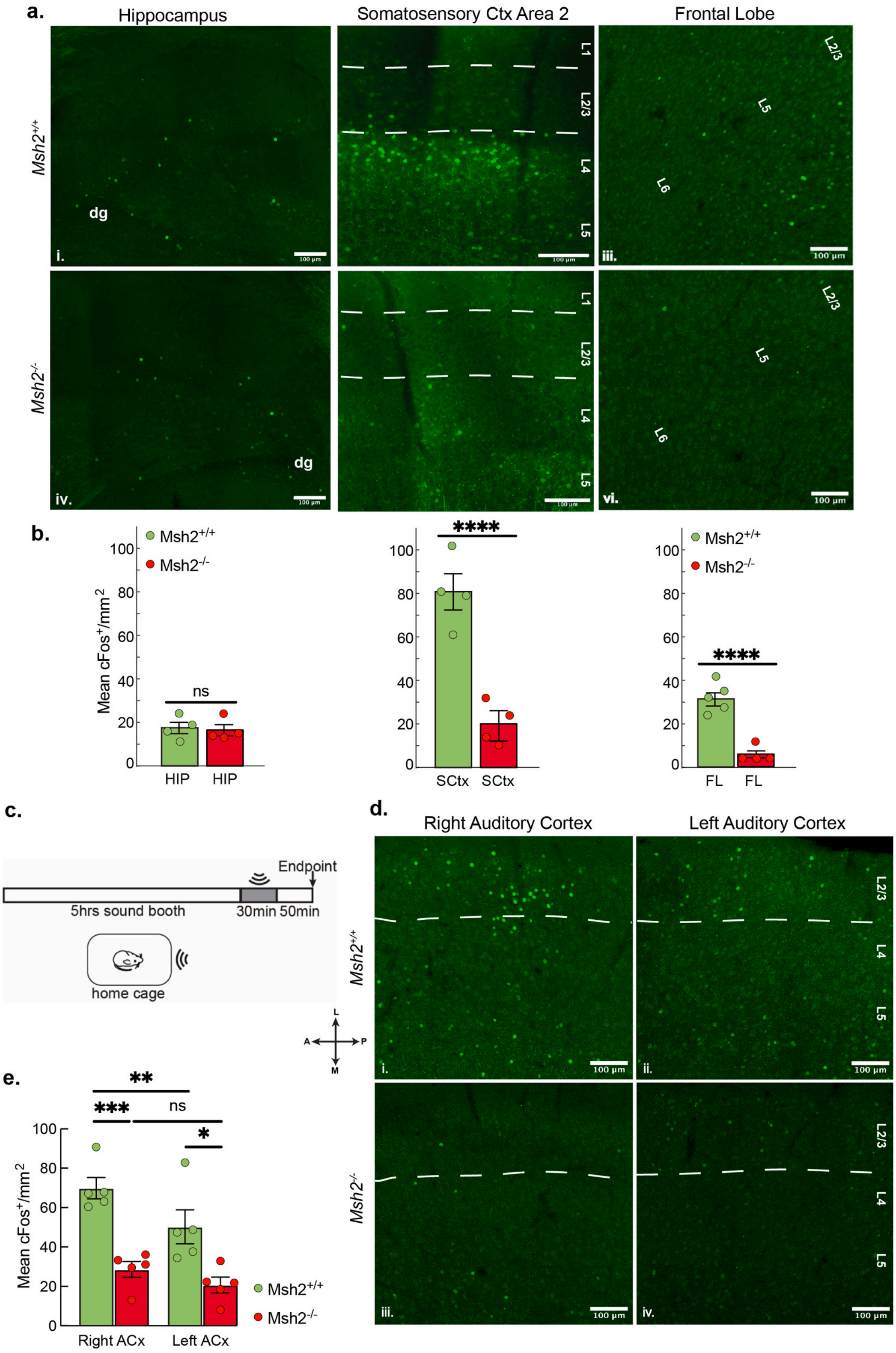

Fig. 1. *c-Fos* expression patterns differ between *Msh2*$^{+/+}$ and *Msh2*$^{-/-}$ mice, showing heterogeneous changes in neural activity across distinct brain regions. **a-b**) No significant difference in c-Fos expression in the hippocampus between the two genotypes (i,iv, b-left population). Significant differences in *c-Fos* between the two genotypes were observed throughout the cortex (ii, v, b-middle: somatosensory cortex; iii, vi, b-right: frontal lobes). N = 4 mice for each genotype. Diminished auditory function in the ACx of *Msh2*$^{-/-}$ mice. **c)** Schematic of sensory function assay utilized: mice were placed in a sound-proof chamber for 5 h to acclimate, given 30 min of auditory stimulation, and then remained in the cage for 50 min post-stimulation prior to perfusion. **d)** *c-Fos* expression in the right and left ACx in *Msh2*$^{+/+}$ (i, ii), and *Msh2*$^{-/-}$ (iii, iv) mice. Dotted lines indicate layers II/III of the cortex. Scale bars are 100 µm. **e)** Population data showing that there are significantly less *c-Fos*$^{+}$ neurons in the right and left ACx of *Msh2*$^{-/-}$ compared to *Msh2*$^{+/+}$ littermates. Statistical analysis was conducted through a Student's two-tailed unpaired *t*-test (*, $p < 0.05$; **, $p \leq 0.001$; ***, $p \leq 0.0001$; n = 5 mice for each genotype, error bars are +/- SEM, center of the error bars represent the mean.) Stereotaxic axis shows anterior-posterior (A/P) and medial–lateral (M/L) axis. Abbreviations: dg = dentate gyrus, HIP = hippocampus, SCtx = somatosensory cortex, FL = frontal lobe.

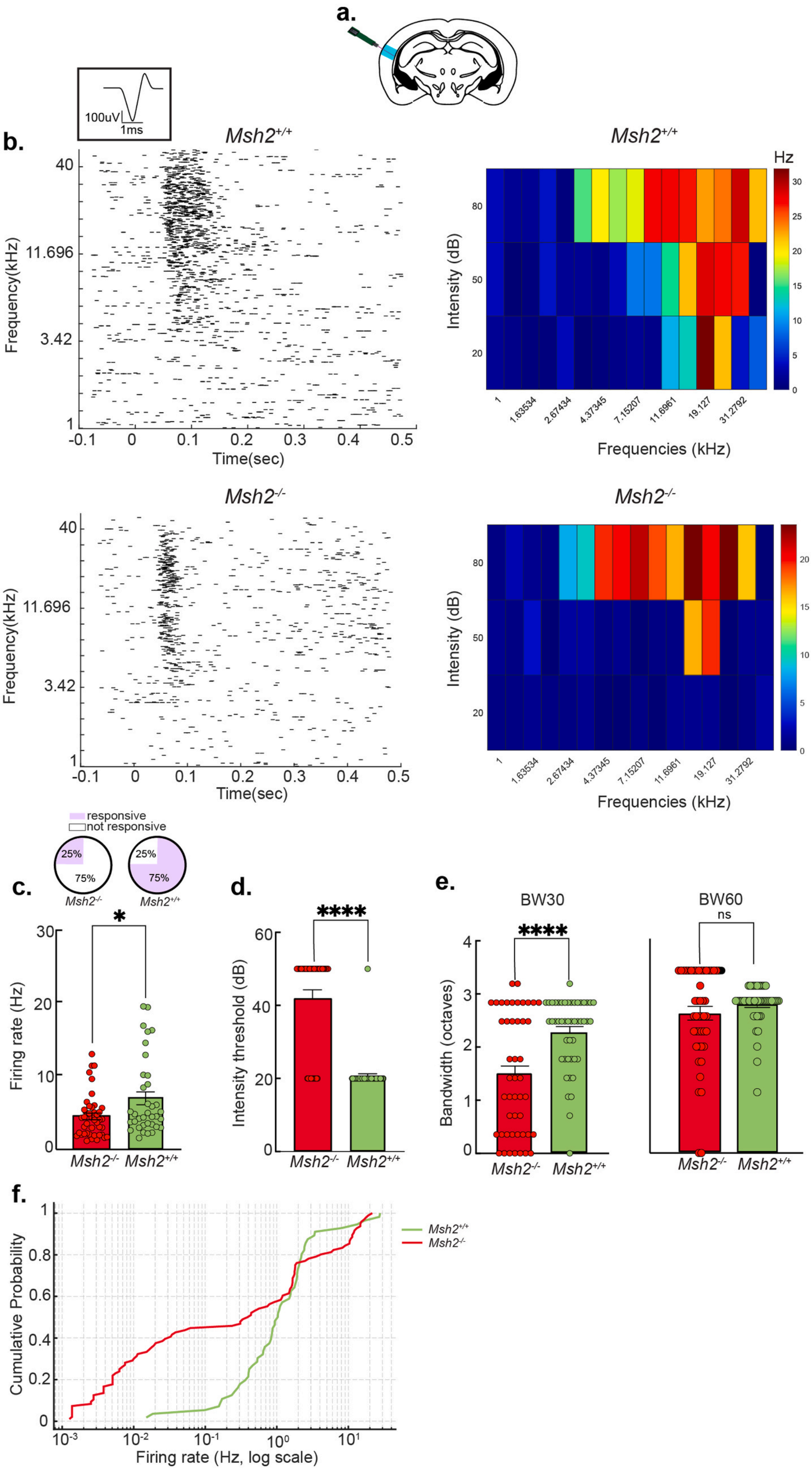

(caption on next page)

Fig. 2. Deficits in frequency response properties in the ACx of *Msh2*$^{-/-}$ mice. **a)** Schematic of experimental paradigm to record from the ACx (shown in cyan) with multi-channel silicone probes. **b)** Representative examples of rasters (left) and tone responsive fields (TRFs; right) from individual clusters of *Msh2*$^{+/+}$ (top) and *Msh2*$^{-/-}$ (bottom) mice. Inset is a representative spike waveform from a putative regular spiking neuron in the ACx. **c)** Proportion of tone-responsive clusters (top), and average firing rate from responsive clusters in *Msh2*$^{+/+}$ and *Msh2*$^{-/-}$ mice (bottom, n = 47 clusters for each genotype; *, p = 0.01). **d)** Average intensity thresholds (dB) from *Msh2*$^{+/+}$ and *Msh2*$^{-/-}$ clusters (n = 47 clusters for each genotype; ****, $p \leq 0.00001$). **e)** Average bandwidths (in octaves) of tuning curves at 30 dB (left; ****, $p \leq 0.00001$) and 60 dB (right) above our lowest intensity level (20 dB) from *Msh2*$^{+/+}$ and *Msh2*$^{-/-}$ clusters (n = 36 clusters for *Msh2*$^{+/+}$ mice; n = 43 clusters for *Msh2*$^{-/-}$ mice). **f)** Cumulative probability of spontaneous firing rate in unstimulated trials (n = 57 clusters for each genotype; $p \leq 0.00001$, Kolmogorov–Smirnov test). N = 2 mice for each genotype, error bars are +/- SEM, center of the error bars represent the mean. (For interpretation of the references to colour in this figure legend, the reader is referred to the web version of this article.)

neural activity in the TRN translates into greater inhibition of its downstream target the MGBv.

To identify potential mechanisms underlying TRN hyperactivity, we examined whether this was associated with molecular deficits within the TRN. Most of the neurons in the TRN express parvalbumin, a calcium binding protein necessary for the regulation of calcium dynamics during neuronal activity (Alberi et al., 2013). Measuring parvalbumin expression serves as a useful metric for identifying plasticity and pathological conditions in the brain (Ruden et al., 2021; Runyan, 2010). Therefore, to screen for TRN deficits in *Msh2*$^{-/-}$ mice, we began with an analysis of parvalbumin expression in PV^{+} neurons. Notably, parvalbumin expression in the TRN of *Msh2*$^{-/-}$ mice was significantly increased compared to *Msh2*$^{+/+}$ (Fig. 4a (i, iv), b (left)). Moreover, quantification of PV^{+} cellular density indicated a significantly higher proportion of PV^{+} neurons compared to total cell count (as indicated by DAPI) in the TRN of *Msh2*$^{-/-}$ mice (Fig. 4b (middle)). This observation is also supported by the higher number of PV^{+} neurons per mm^{2} of TRN in *Msh2*$^{-/-}$ compared to *Msh2*$^{+/+}$, whereas the number of DAPI^{+} cells per mm^{2} of TRN is similar between the two genotypes (Fig. 4b (right)). These data indicate that PV^{+} neurons in the TRN of *Msh2*$^{-/-}$ mice are more numerous and exhibit increased parvalbumin expression compared to *Msh2*$^{+/+}$ controls. Upon further investigation we also observed that, on average, PV^{+} neurons in *Msh2*$^{-/-}$ mice exhibited a larger cellular area compared to their *Msh2*$^{+/+}$ littermates (Fig. 5a). This phenotype was specific to the TRN and was not observed in PV^{+} neurons in the ACx of *Msh2*$^{-/-}$ mice (Fig. 5b, e).

Collectively, these abnormal cellular phenotypes prompted us to investigate whether functional features crucial for the TRN's electrical properties were also affected. This could directly contribute to the disruption of thalamo-cortical sensory evoked responses we observed. PV^{+} neurons in the TRN are electrically coupled via connexin-36 (Cx36) gap junctions (Landisman, 2002). Therefore, we examined the expression of Cx36 in PV^{+} neurons to determine how the TRN's role as a modulator of TC activity could be compromised in *Msh2*$^{-/-}$. Like most connexins, Cx36 typically does not remain as a single-unit membrane protein but assembles into connexons- six-protein hemichannels that permit the direct transfer of ions and small molecules between cell bodies (Saez et al., 2003). To quantify connexon formation, we measured fluorescence intensity and puncta count per micron of somatic perimeter, which reflect the assembly of proteins. In *Msh2*$^{-/-}$ TRN, we observed a significant decrease in Cx36 puncta per micron in PV^{+} neurons (Fig. 5c). We also found an increase in Cx36 fluorescence intensity (Fig. 5d). This increase was attributed to the formation of aggregates, resulting in Cx36 plaques. These changes in Cx36 were specific to the TRN and were not observed in the ACx of *Msh2*$^{-/-}$ mice. The evidence suggests that in *Msh2*$^{-/-}$ mice, PV^{+} neurons in the TRN show altered Cx36 proteodynamics. This disrupted gap junction formation, and consequently interneuron coupling, could compromise the TRN's modulation of thalamo-cortical activity.

Our observations of high parvalbumin levels and abnormal connexin clustering in *Msh2*$^{-/-}$ mice suggest abnormalities in the electrical properties of the TRN, potentially causing the observed downstream dysfunction in auditory processing. To investigate this, we performed in vivo recordings from the auditory TRN, confirmed by tone-evoked responses detected in a subset of clusters (Fig. 6a-b). To assess possible deficits in intrinsic electrophysiological properties, we examined spontaneous activity. The TRN has two characteristic firing patterns: tonic and bursting (Hartings et al., 2003). Using anesthetized mice, we investigated whether these firing patterns were altered with the loss of *Msh2* by quantifying properties of the interspike interval (ISI). One of the most striking phenotypes in *Msh2*$^{-/-}$ was a higher proportion of short ISIs compared to *Msh2*$^{+/+}$ (Fig. 6c-d). This suggests that in the TRN of *Msh2*$^{-/-}$ mice, burst firing epochs become the predominant mode of output, with bursts showing higher spike rates. We also quantified the variability of spike trains using the coefficient of variation of ISIs metric (Cv2). Cv2 can range between 0 and 2, with higher values indicating higher variability in ISIs. Quantifying Cv2 for both *Msh2*$^{+/+}$ and *Msh2*$^{-/-}$ clusters, we found greater variability in the timing of action potentials in spike trains from *Msh2*$^{-/-}$ mice (Fig. 6e-f). If the increased burst firing in the TRN of *Msh2*$^{-/-}$ mice reflects stronger electrical coupling mediated by Cx36 plaques, this enhanced connectivity would promote greater synchronous activity between neighboring TRN clusters. To test this, we quantified spike-time synchrony between TRN neurons using cross-correlation analysis. In the TRN, electrical coupling typically gives rise to spike correlations occurring within a narrow 3–5 ms time window (Mendoza et al., 2022). Notably, we found spiking activity among neighboring TRN clusters in *Msh2*$^{-/-}$ mice showed nearly 50 % higher cross-correlation compared to *Msh2*$^{+/+}$ (Fig. 6g). These findings indicate that the coupling and discharge patterns of the TRN, which are essential for generating oscillations and contribute significantly to brain rhythms (Steriade et al., 1987; Pinault, 2004; Bartho, 2014; McAlonan et al., 2006), become disrupted in the absence of MSH2.

TRN dysfunction is associated with increased oxidative damage

Collectively, the abnormally high levels of PV, enlarged cell body, connexin plaques, and aberrant electrical activity in the TRN suggest cellular stress caused by the absence of *Msh2*. Because *Msh2* deficiency is associated with increased oxidative DNA lesions (Russo, 2009), we hypothesized that the impaired neural function in *Msh2*$^{-/-}$ mice could reflect accumulation of oxidative damage in TRN neurons. Oxidative lesions can arise from reactive oxygen species (ROS) generated during normal cellular metabolism (Okuno et al., 2012); in the absence of Msh2, oxidized DNA may not be efficiently repaired and may therefore accumulate. To obtain a comprehensive assessment of oxidative DNA and cellular damage, we used two complementary markers: 8-oxo-dG and acrolein. 8-oxo-dG serves as a direct indicator of oxidative modification to DNA bases, reflecting damage specific to nucleic acid. In contrast, acrolein, a reactive aldehyde generated during lipid peroxidation, marks broader oxidative stress affecting proteins, lipids, and nucleic acids. PV^{+} neurons in the *Msh2*$^{+/+}$ TRN showed no detectable 8-oxo-dG signal above background, whereas in *Msh2*$^{-/-}$ there was clear 8-oxo-dG staining (Fig. 7a). Compared to the baseline fluorescence intensity in *Msh2*$^{+/+}$, PV^{+} neurons in *Msh2*$^{-/-}$ had significantly higher 8-oxo-dG intensity indicating higher levels of oxidized DNA (Fig. 7b). For the acrolein assay, a detection threshold was established based on the *Msh2*$^{-/-}$ signal distribution (see Methods), as *Msh2*$^{+/+}$ showed occasional visible acrolein immunoreactivity (Fig. 7c) that warranted inclusion only when above this threshold. When we applied the *Msh2*$^{-/-}$ threshold criteria to the TRN of *Msh2*$^{+/+}$ mice, fewer cells passed threshold to be detected as acrolein-positive. Additionally, the few cells that were detected in *Msh2*$^{+/+}$ TRN had significantly lower acrolein

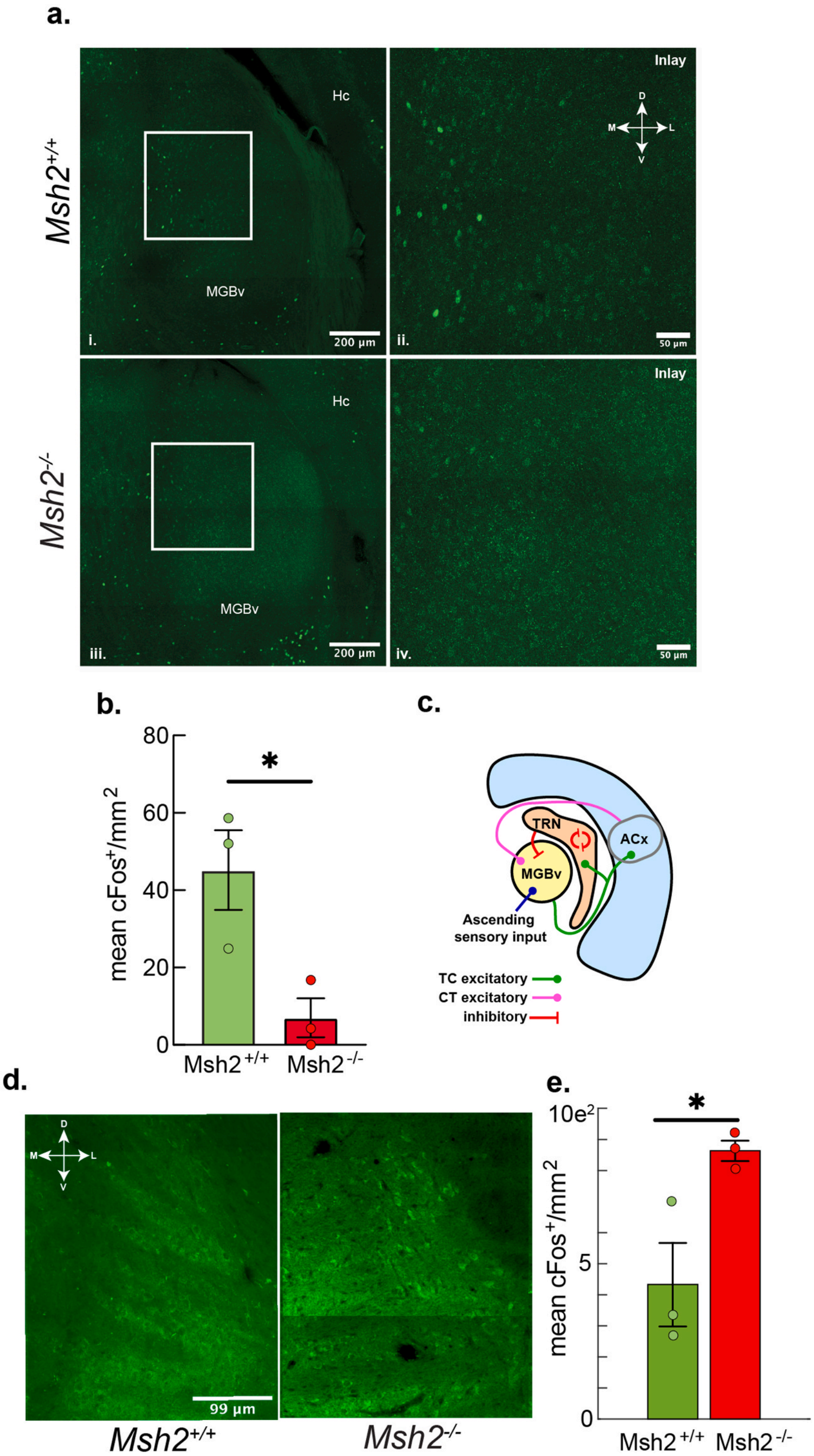

Fig. 3. Divergent changes in neural activity in the MGBv and TRN of sweep stimulated *Msh2*$^{-/-}$ and *Msh2*$^{+/+}$ mice. **a)** Quantification of c-Fos^{+} neurons in the MGBv of *Msh2*$^{+/+}$ (top, i-ii) and *Msh2*$^{-/-}$ (bottom, iii-iv) mice. Scale bars indicate 200 μm and 50 μm for the inlay. **b)** Statistical analysis of MGBv c-Fos^{+} neurons (n = 3 mice for each genotype; *, $p < 0.05$). **c)** Diagram of TRN connectivity; excitatory TC connections from the MGBv send collaterals to the TRN and form reciprocal excitatory connections with the cortex. The TRN provides inhibitory signaling to the thalamus and itself. **d)** Increase in sound evoked neural activity in the TRN of *Msh2*$^{-/-}$ mice and **e)** statistical analysis (n = 3 mice for each genotype; *, $p < 0.05$). Stereotaxic axis represents the medial–lateral (M/L) and dorso-ventral (D/V) axis; Hc = hippocampus. Error bars are +/- SEM, center of the error bars represent the mean. Statistical analysis conducted through a Student's two-tailed unpaired *t*-test.

intensity compared to the *Msh2*$^{-/-}$ TRN (Fig. 7d). Cells in the ACx of the *Msh2*$^{-/-}$ and *Msh2*$^{+/+}$ mice did not pass threshold for acrolein detection and had only background levels of 8-oxo-dG and therefore did not meet criteria for quantification (Supplementary Fig. 2). Hence, the elevated 8-oxo-dG and acrolein signals in the *Msh2*$^{-/-}$ TRN indicate increased oxidative damage consistent with a higher oxidative stress burden/redox imbalance in this region, with no comparable change observed in ACx. These findings support the interpretation that loss of *Msh2* may

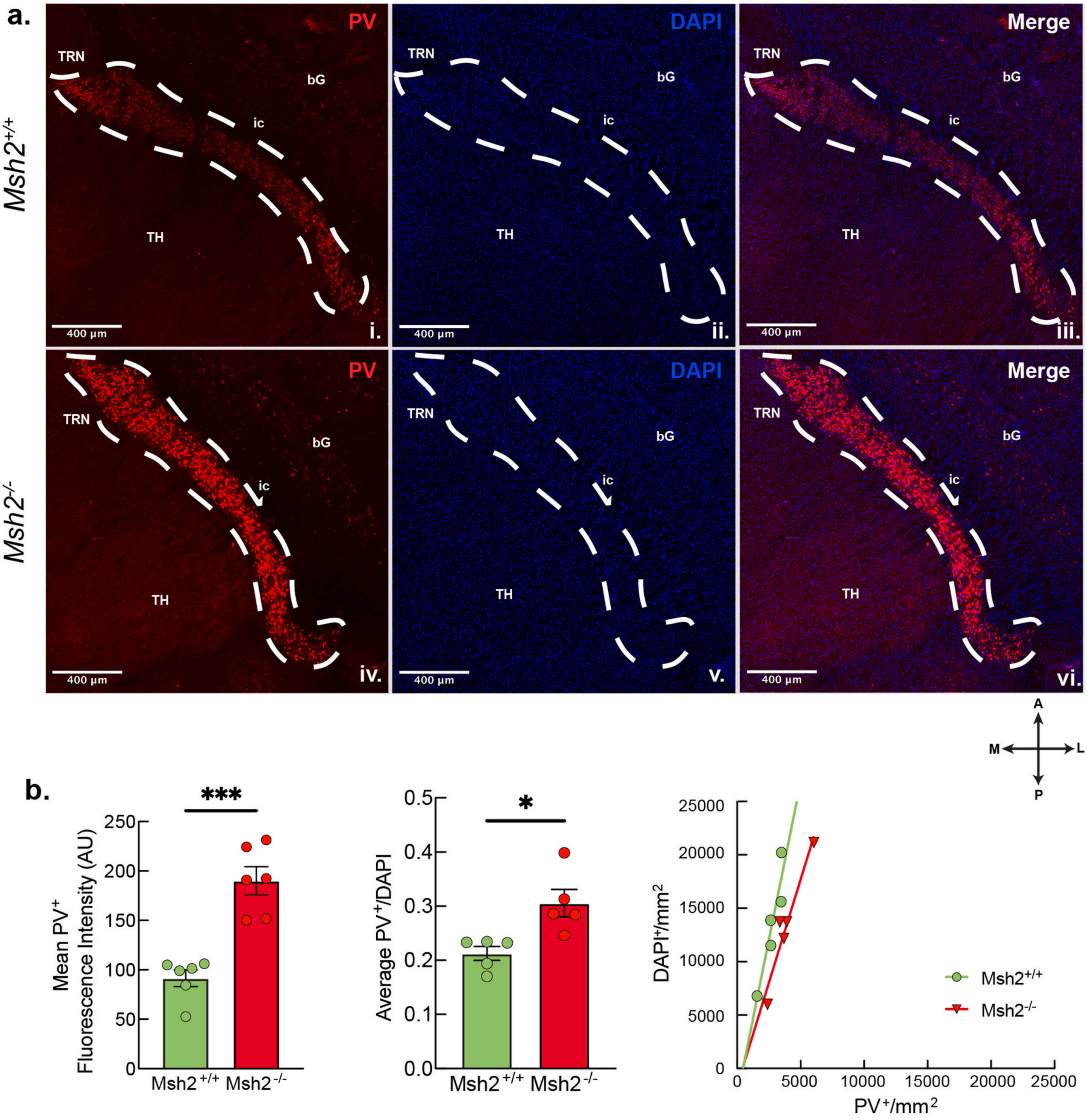

Fig. 4. Greater parvalbumin expression within the TRN of *Msh2*$^{-/-}$ mice. **a)** Parvalbumin (PV^{+}) staining counterstained with DAPI in the TRN of *Msh2*$^{+/+}$ (top, i-iii) and *Msh2*$^{-/-}$ (bottom, iv-vi) mice. Scale bars represent 400 µm. **b) Left**: Mean fluorescence intensity in arbitrary units (AU) (***, $p = 0.0001$, $n = 6$ mice for each genotype), **middle**: average PV^{+} neurons per DAPI-demarcated cells (*, $p < 0.05$, $n = 5$ mice for each genotype), and **right**: relative density of PV^{+} neurons in *Msh2*$^{+/+}$ and *Msh2*$^{-/-}$ mice ($n = 5$ mice for each genotype). Error bars represent SEM. Statistical analysis was conducted through a Student's unpaired two-tailed *t*-test. Stereotaxic axis (lower right) represents anterior-posterior (A/P) and medial–lateral (M/L) axis. TH = thalamus, bG = basal ganglia, ic: internal capsule, TRN = thalamic reticular nucleus. Error bars are +/- SEM, center of the error bars represent the mean.

lead to altered TRN function as a result of oxidative stress or oxidative DNA damage (Russo, 2009; Colussi, 2002; Martin, 2010).

Discussion

We observed sensory deficits in the absence of MSH2, an essential protein in MMR, using a genetic knockout of *Msh2* in mice. Compared to wildtype littermates, *Msh2*$^{-/-}$ mice showed widespread reductions in spontaneous cortical activity and reduced sound-evoked responses in both the ACx and MGBv. In contrast, the TRN showed abnormally bursty and hypersynchronous neural activity accompanied by elevated PV expression. Within the TRN, PV^{+} neurons displayed enlarged somata, and increased Cx36 fluorescence and puncta aggregation-indicative of enhanced gap-junction plaque formation. These functional and structural abnormalities were paralleled by elevated levels of 8-oxo-dG and acrolein, markers of oxidative stress, specifically within the *Msh2*$^{-/-}$ TRN.

In response to frequency modulated sweeps, *Msh2*$^{+/+}$ mice showed right ACx lateralized neural activity (indicated by *c-Fos*$^{+}$ neurons) in the superficial cortical layers, consistent with findings from previous studies

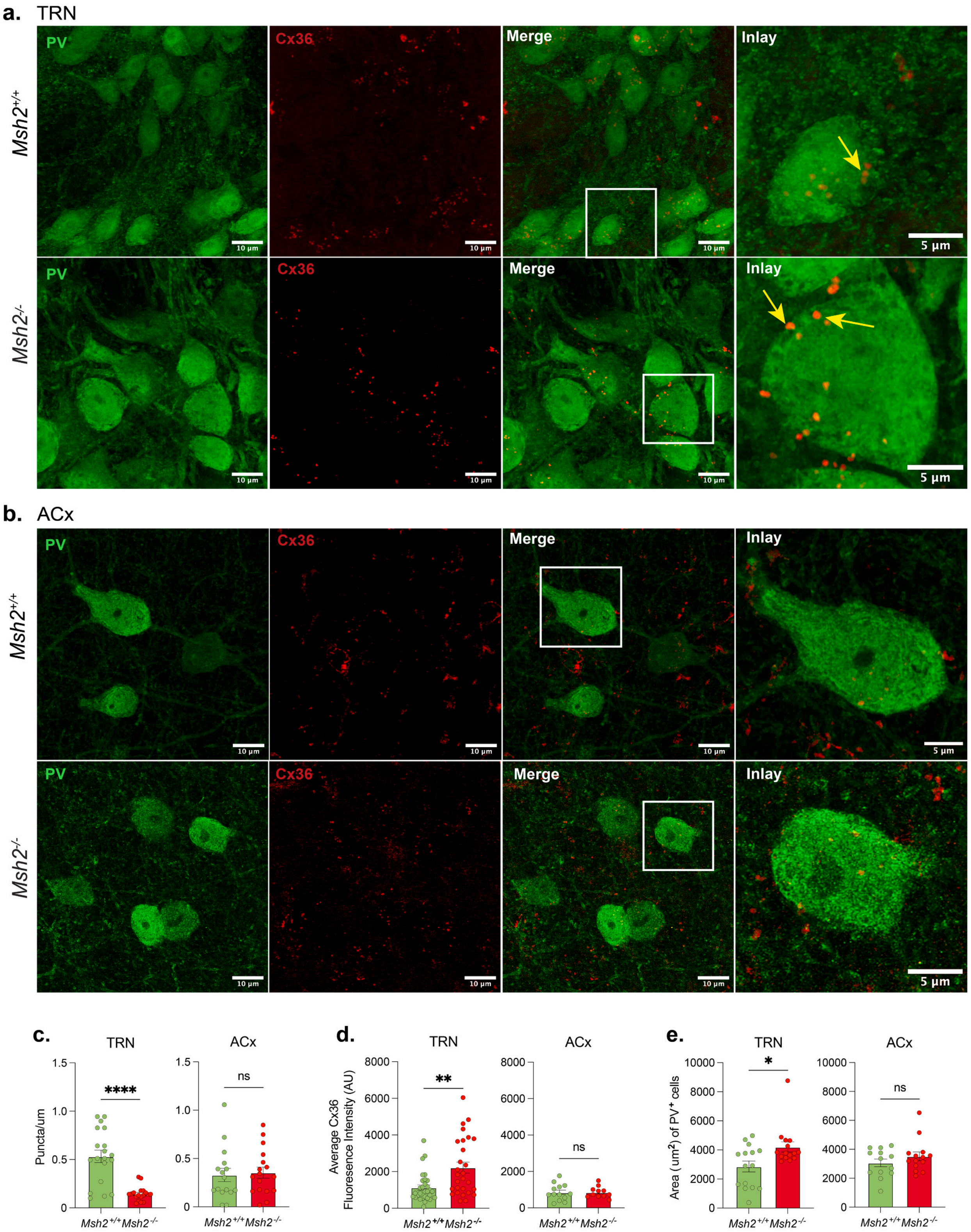

Fig. 5. Cellular and molecular abnormalities in PV$^+$ TRN neurons of *Msh2*$^{-/-}$. PV$^+$ and Cx36 staining in **a)** TRN and **b)** auditory cortices of *Msh2*$^{+/+}$ and *Msh2*$^{-/-}$ mice. **c)** The formation of Cx36-containing plaques in *Msh2*$^{-/-}$ PV$^+$ neurons led to a decrease in puncta/μm in the TRN (****, $p \leq 0.0001$, $n = 3$ mice for each genotype; neurons analyzed: 19 from *Msh2*$^{+/+}$ and 18 from *Msh2*$^{-/-}$), but not the ACx (neurons analyzed: 16 from *Msh2*$^{+/+}$ and 17 from *Msh2*$^{-/-}$). **d)** Cx36 fluorescence intensity (AU) was found to be higher in *Msh2*$^{-/-}$ TRN (**, $p \leq 0.01$, $n = 3$ mice for each genotype; neurons analyzed: 30 from *Msh2*$^{+/+}$ and 28 from *Msh2*$^{-/-}$), but comparable in the ACx of both genotypes (neurons analyzed: 13 from *Msh2*$^{+/+}$ and 11 from *Msh2*$^{-/-}$). **e)** PV$^+$ cells in the TRN were also larger in *Msh2*$^{-/-}$ animals (*, $p \leq 0.05$, $n = 3$ mice for each genotype; neurons analyzed: 15 from *Msh2*$^{+/+}$ and 15 from *Msh2*$^{-/-}$), but not the ACx (neurons analyzed: 13 from *Msh2*$^{+/+}$ and 14 from *Msh2*$^{-/-}$). Statistical analysis was conducted through Student's two-tailed unpaired *t*-test. All error bars are standard error of the mean (SEM). Scale bars represent 10 μm and 5 μm (inlay). Error bars are +/- SEM, center of the error bars represent the mean.

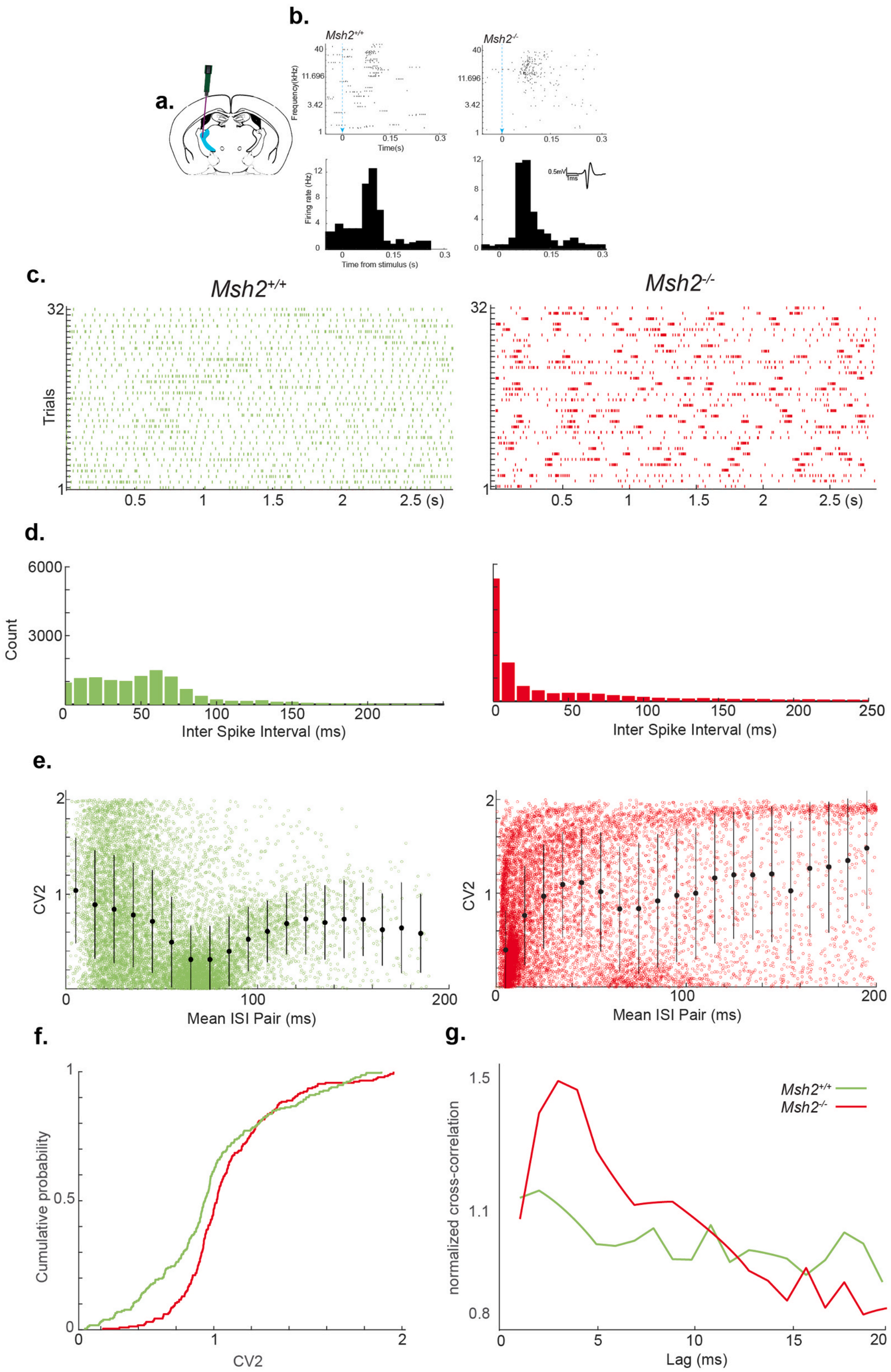

Fig. 6. Higher incidence of burst firing in the TRN of *Msh2*$^{-/-}$ mice. **a)** Schematic of experimental paradigm to record spontaneous activity from the TRN (shown in cyan) in *Msh2*$^{+/+}$ and *Msh2*$^{-/-}$ mice. **b)** Confirmation of auditory TRN recording site based on tone-evoked responses. **c)** Representative examples of rasters from *Msh2*$^{+/+}$ (left) and *Msh2*$^{-/-}$ (right) clusters. Inset is a representative spike waveform from a putative interneuron in the TRN. **d)** Histogram of inter-spike intervals (ISIs) from *Msh2*$^{+/+}$ (left) and *Msh2*$^{-/-}$ (right) clusters. **e)** Cv_2 values from *Msh2*$^{+/+}$ (left) and *Msh2*$^{-/-}$ (right) clusters. Bin sizes are 10 ms. **f)** *Msh2*$^{-/-}$ clusters have significantly higher Cv2 values than *Msh2*$^{+/+}$ clusters ($p < 0.05$). **g)** Cross-correlation between spike trains in each genotype. N = 2 mice for each genotype; error bars are +/- SD, center of the error bars represent the mean. (For interpretation of the references to colour in this figure legend, the reader is referred to the web version of this article.)

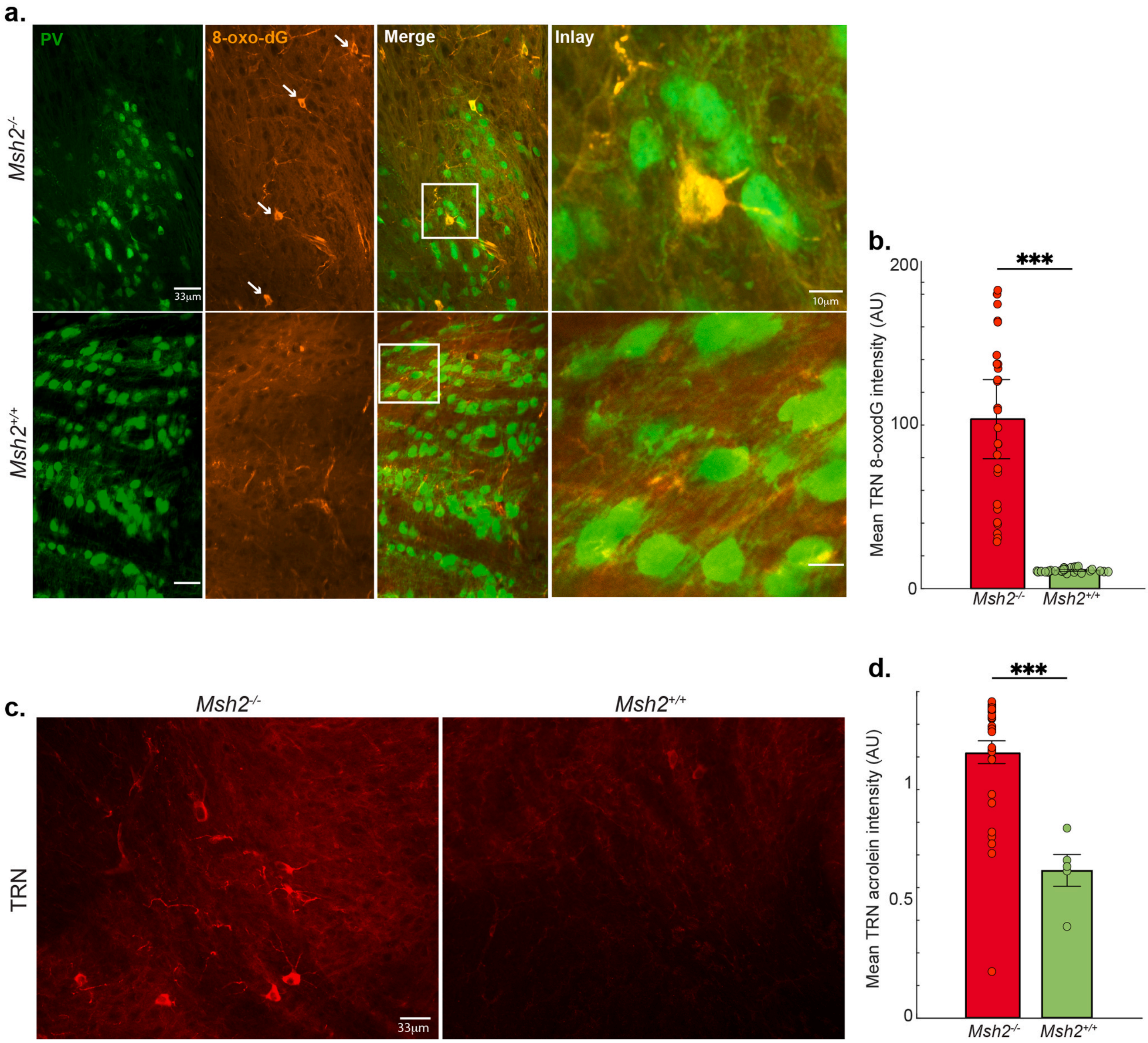

Fig. 7. Increased oxidative DNA and cellular damage in the TRN of *Msh2*$^{-/-}$ mice. **a**) Representative staining for 8-oxo-dG in TRN PV^{+} neurons. **b**) Quantification of mean 8-oxo-dG fluorescence intensity in PV^{+} neuronal somata shows a significant increase in *Msh2*$^{-/-}$ compared to *Msh2*$^{+/+}$ (AU arbitrary units; *** $p \leq 0.0001$). **c**) Representative acrolein staining in the TRN reveals a greater number of cells with elevated acrolein signal in *Msh2*$^{-/-}$ mice relative to Msh2$^{+/+}$. **d**) Mean acrolein fluorescence intensity in the TRN is significantly higher in *Msh2*$^{-/-}$ mice (*** $p \leq 0.0001$). Data are shown as mean ± SEM; $n = 4$ mice per genotype. Statistical comparisons were performed using an unpaired two-tailed Student's *t*-test. Scale bars: 33 µm (main panels) and 10 µm (inlays).

(Levy, 2019; Wetzel et al., 2008; Wetzel et al., 1998). In *Msh2*$^{-/-}$, this stimulus-driven response is considerably reduced in the right and left ACx. Using multiunit recordings of neural activity from the ACx, we examined the deficits in stimulus-driven responses in more detail. We found deficits in frequency tuning across multiple metrics in *Msh2*$^{-/-}$ mice compared to their wildtype littermates as well as lower spontaneous activity. Indicative of a diminished response to sounds, fewer clusters in *Msh2*$^{-/-}$ mice were responsive to tones, and the average firing rate of these responsive clusters was lower, with significantly higher intensity thresholds. Additionally, the dynamic range of their frequency response bandwidth was significantly reduced. To identify the origin of these deficits, we investigated the ascending auditory pathways. Our findings revealed a decrease in sound evoked neural activity in the MGBv but not the inferior colliculus. Based on these findings, we reasoned that the potential sound processing deficits originated within the thalamus. We identified cellular and electrophysiological pathologies in the TRN, which plays a crucial role in modulating thalamocortical pathways and serves as a major source of inhibition for the thalamus. Although we focused on auditory structures, the reduction in basal activity we observed in somatosensory and frontal cortices (Fig. 1) indicates that the impact of *Msh2* loss is not restricted to auditory processing. Instead, these findings are consistent with a more widespread TRN dysfunction, because even unstimulated cortical regions showed a lower gain in their spontaneous activity. This pattern is consistent with the idea that different portions of the TRN, while not strictly unimodal, influence the excitability of the thalamo-cortical circuits with which they are most strongly connected. Dysfunction of the TRN has been shown to be linked to neurological disorders with sensory abnormalities, insomnia, and schizophrenia (Li, 2020).

While we do not discount the possibility of dysfunction in other brain regions resulting from *Msh2* loss, and therefore MMR reduction, our findings pose a fundamental question about the specific vulnerability of the affected PV^{+} neurons in the TRN. PV^{+} interneuron dysfunction is frequently associated with a multitude of nervous system diseases (Ruden et al., 2021; Cernotova et al., 2023; Filice et al., 2016; Wohr, 2015; Godoy et al., 2022; Schwaller, 2004; Nahar et al., 2021). This susceptibility can be attributed to a combination of factors, including genomic instability, high firing rates, and the unique vulnerability of PV^{+} neurons to a variety of stressors. The TRN is particularly vulnerable, largely because of its predominantly PV^{+} population and its distinction of having some of the highest firing rates in the brain, with firing epochs reaching up to 500 spikes per second (Hartings et al., 2003; Marlinski and Beloozerova, 2014). As a result, PV^{+} neurons in the TRN have extraordinary energy requirements to support their firing activity and provide defense against substantial glutamatergic stress. One of the key protective mechanisms employed by these neurons involves regulating calcium buffering through parvalbumin levels (Caillard, 2000). Our results suggest that neurons in the TRN appear to be in a high calcium buffering state as evidenced by significantly increased intensity of parvalbumin immunoreactivity (Fig. 4b (left)). Moreover, increases in intracellular calcium levels can lead to the induction of DNA damage from reactive oxygen species, which cannot be repaired efficiently in the absence of MSH2 (Russo, 2009; Colussi, 2002; Crowe et al., 2006). This exacerbates the impact of genomic instability on the TRN.

We also observed increased gap junction plaque formation in the TRN of *Msh2*−/− mice compared to the *Msh2*$^{+/+}$ TRN and ACx of both genotypes, suggesting that *Msh2*-deficiency specifically affects the TRN. Connexins are highly dynamic membrane proteins with very short half-lives, lasting only a few hours (Wang et al., 2015). The coordination of connexin trafficking and assembly is managed through phosphorylation events controlled by numerous scaffolding proteins and various kinases (Wang et al., 2015). Genomic instability can perturb these regulatory mechanisms leading to disruptions in the binding of scaffolding proteins like zona occludens-1 (ZO-1) and an increase in gap junction plaques (Roh and Funderburgh, 2011; Hunter and Gourdie, 2008). While these mechanisms have primarily been examined in the context of Cx43 due to its extensive study, the biochemical interactions between ZO and Cx36, the connexin type in the TRN, are well-established (Li, 2004). Disruptions in these interactions could, therefore, have similar impacts in the TRN. DNA damage response elements and cellular stress also lead to an increase in the activity of protein kinase C, Akt, MAPK and src kinase, which are all known to phosphorylate connexins and result in an increase in gap junction plaque size and internalization from the plasma membrane (Shin et al., 2022; Pogoda et al., 2016). Interestingly, an increase in Akt activity could also play a role in the higher density of PV^{+} neurons we observed in the TRN (Fig. 4a-b). Akt is a key regulator of neuronal survival, and its overexpression has been shown to prevent apoptosis in postnatal brain development (Dudek, 1997). More relevant to our study, deleting antagonists of Akt activity significantly enhances the survival of postmitotic neurons derived from the medial ganglionic eminence (Wong, 2018).

Previous experimental and theoretical studies have elucidated the significance of gap-junctional coupling in mediating burst firing in neural networks (Coombes and Zachariou, 2009; Perez-Velazquez et al., 1994; Skinner et al., 1999; Zhang, 1998). An increase in Cx36 gap junction plaques could enhance local coupling between PV^{+} neurons in the TRN of *Msh2*$^{-/-}$ mice (Lee, 2021). Enhanced electrical coupling has been shown to increase the synchrony of spiking activity in neural networks (Shosaku and Sumitomo, 1983). Recordings of spontaneous TRN activity revealed more frequent bursting epochs, shorter ISIs, and higher cross-correlation between neighboring clusters in *Msh2*$^{-/-}$ mice, consistent with enhanced electrical coupling (Fig. 6). Furthermore, the significantly higher Cv2 values observed in the firing discharge of the *Msh2*$^{-/-}$ TRN align with theoretical findings that spike bursts exhibit greater Cv2 values and variability in spike timing (Svirskis and Rinzel, 2000). Given that the TRN is an inhibitory nucleus, stronger synchronization of its discharge could more effectively reduce activity in both the MGBv and ACx (Fig. 3c) (Li, 2024). This aligns with our observations that increased synchronized TRN activity in *Msh2*$^{-/-}$ mice is observed alongside with reduced sound evoked responses in the ACx and MGBv (Figs. 1-3). Another factor that could contribute to the abnormal neural activity we observed in the TRN is increased parvalbumin expression, which has been shown to induce a change in firing patterns from regular to burst firing (Roussel et al., 2006; Bischop et al., 2012). Consistent with this finding, burst firing in TRN neurons has been shown to be significantly altered in PV-KO mice compared to WT animals. In PV-KO mice, TRN neurons exhibited bursting epochs with prolonged ISIs compared to WT mice (Alberi et al., 2013). These observations complement our findings, as we observed that higher levels of PV in *Msh2*$^{-/-}$ mice correlated with shorter ISIs compared to *Msh2*$^{+/+}$ mice (Fig. 6d). Relatedly, the increase in burst firing epochs we observed in the TRN of *Msh2*$^{-/-}$ mice could also contribute to the PV^{+} interneuron swelling. Bursts of action potentials increase the influx of calcium and sodium ions into the intracellular space (Fig. 5), potentially contributing to cellular edema (Rungta, 2015). A synergistic model that could account for the atypical firing properties in the TRN of *Msh2*$^{-/-}$ mice is one where stronger electrical coupling synchronizes neuron groups and altered calcium handling (via altered PV levels) and cell-intrinsic properties make each neuron more prone to burst in response to inputs.

To delve deeper into the cellular pathologies underlying TRN dysfunction, we assessed oxidative damage using two complementary markers acrolein and 8-oxo-dG (Okuno et al., 2012). Acrolein, a lipid peroxidation-derived aldehyde and marker of ROS-mediated oxidation, was significantly higher in the TRN of *Msh2*$^{-/-}$ mice compared to *Msh2*$^{+}$/$^{+}$ (Fig. 7). Since MSH2 is responsible for repairing base–base mismatches and insertion-deletion loops (Liu et al., 2017), its loss likely results in the accumulation of unrepaired DNA lesions, increasing the oxidative damage burden/redox imbalance (Kang et al., 2012). The resulting oxidative stress promotes both lipid oxidation, reflected by increased acrolein, and direct oxidative modification of DNA bases, reflected by 8-oxo-dG (Juan et al., 2021). Together, these markers describe the dual impact of *msh2* loss: primary oxidative DNA damage and secondary lipid-derived oxidative by-products. In *Msh2*$^{-/-}$ cells, the accumulation of oxidized DNA bases suggests that elevated oxidative stress is causing DNA damage that necessitates repair (Russo, 2009; Colussi, 2002; Martin, 2010). The sustained oxidative stress overwhelms repair capacity and may trigger neuroinflammatory responses, ultimately compromising TRN integrity and function (Zhang, 2024). Activation of neuroinflammatory pathways could have also contributed to the neuronal swelling observed in PV^{+} neurons (Anderson et al., 2023). Finally, these cellular disruptions also have the potential to impact the function of other key players in TRN burst generation: T-type calcium channels and membrane resting potential (Huguenard and Prince, 1992). The intricate interplay of these factors creates a delicate balance within PV^{+} neurons, which can quickly tip towards the development of pathological conditions.

In conclusion, our findings suggest that *Msh2* plays an important role in the maintenance of normal sensory processing. We have identified a potential involvement of *Msh2* in modulating the cortico-reticulo-thalamic circuit through the regulation of PV^{+} interneuron function. Future studies will elucidate the precise molecular mechanisms by which MMR promotes the development or maintenance of TRN neurons and provide valuable insights into how the brain utilizes DNA repair mechanisms for normal function.

Methods

Msh2-deficient mice (*Msh2*$^{-/-}$) were a gift from H. te Riele. All mice were at least 8 weeks of age. All procedures follow vertebrate animal protocols approved by CCNY IACUC.

Auditory stimulation

Mice were placed individually into a sound-attenuated booth. All mice were provided with water, food, and air circulation. The mice remained in the booth for at least 5 h before being presented with a free-field stimulation (Avisoft Bioacoustic speakers, Glienicke Germany) of frequency modulated (FM) up and down sweeps of 1–40 kHz at 2 octaves/sec. The stimuli were 2 s long and separated by an interval of 18 s of silence between the end of one stimulus and the beginning of another. This procedure continued for 30 min in total. After stimulation, the mice were kept in the sound booth for an additional 50 min post-stimulation prior to perfusion.

Preparation of brain sections

Mice were given an intraperitoneal (IP) injection of ketamine (75 mg/kg) and medetomidine (0.5 mg/kg) in 0.9 % NaCl. After anesthesia was confirmed by the absence of a reflexive twitch, mice were perfused intracardially with 15 mL of ice-cold phosphate buffered saline (PBS, 137 mM NaCl, 2.7 mM KCl, 10 mM Na_2HPO_4, 1.8 mM KH_2PO_4). Mice were then perfused with 20 mL of 4 % paraformaldehyde (PFA, Alfa Aesar). Post perfusion, mice were decapitated and dissected brains were placed in 4 % PFA to post-fix for 48 h. 50 μm free floating sections were prepared on a vibratome on a horizontal or coronal plane.

Immunohistochemistry

Sections were washed with PBS (3x for 15 min) at room temperature (RT) and gently rocked for each wash before being blocked (5 % goat serum, 0.3 % TritonX-100 in PBS) for 2 h at RT. Following blocking, sections were incubated in primary antibodies (anti-parvalbumin, Sigma-Aldrich, P3088, 1:500; anti-parvalbumin, Cell Signaling, E8N2U, 1:1,000; anti-c-Fos, Synaptic Systems, 226–008, 1:2,000; anti-cx36, ThermoFisher Scientific, 37–4600, 1:250; anti-acrolein, Abcam, AB240918, 1:200 at 4 °C overnight, and anti 8-oxo-dG, JaICA/Nikken MOG-100P, 1:100 at 4 °C 48 h. We performed an RNAse and HCl antigen retrieval step for the 8-oxo-dG immunohistochemistry. Sections were then washed with PBS (4x for 15 min) and then incubated with secondary antibodies for 2 h at RT (Alexa-Fluor 546, Alexa-Fluor 488). Unbound secondary antibody was washed in PBS (3x for 15 min) at RT. A subset of sections were then counterstained with 4′,6-diamidino-2-phenylindole (DAPI) in PBS (1 μg/ml) for 15 min after the final wash of PBS. Sections were then mounted using Fluoromount-G (eBioscience) and imaged through confocal microscopy (Zeiss LSM 800/Zeiss LSM 880).

Cellular quantification/analysis

Quantification of c-Fos immunohistochemistry was conducted utilizing Fiji/ImageJ. All images were subject to consistent parameters during the imaging process, such as the same exposure time, Z-stack intervals, and post-processing/editing in Fiji. Quantification of *c-Fos*-positive cells was performed by selecting a region of interest, *c-Fos*-positive cells were then counted using the Cell Counter plugin available on ImageJ/Fiji. Because *c-Fos* staining labeled the majority of TRN neurons in both genotypes, we used a modified analysis pipeline. To ensure objective and reproducible detection, we first used the ImageJ Analyze Particles module to define thresholding and size parameters based on *Msh2*$^{-/-}$ TRN tissue. We then applied these identical parameters to the *Msh2*$^{+/+}$ TRN images collected in the same imaging session with identical confocal imaging settings.

Quantification of PV-positive (PV^+) cells was conducted by choosing 3 representative regions of interest (ROI) and manually counting all PV^+ cells in that region. Cell count was then divided by the area (mm^2) and averaged over 3 regions. Quantification for cellular fluorescence was conducted by selection of 50 representative cells. Background fluorescence was subtracted from measured integrated density and averaged over 50 cells. Quantification for PV^+-specific connexin staining was conducted with CellProfiler, by creating a mask of PV-cells and only measuring puncta fluorescence in aforementioned masked PV^+-cells, removing background fluorescence by using non-PV^+ cell tissue as a baseline, running an Otsu three-class threshold, and normalizing by area of the cell. Connexin puncta density was expressed as puncta per unit of somatic perimeter length (puncta/μm) to account for their membrane-associated localization and genotype-dependent differences in soma size.

Quantification of acrolein and 8-oxo-dG fluorescence between the two genotypes was also conducted with the same exposure time, Z-stack intervals, and post-processing/editing in ImageJ. Acrolein analysis in the TRN was also performed with CellProfiler. Acrolein-positive cells were readily identifiable in the TRN of *Msh2*$^{-/-}$ mice (Fig. 7c); therefore, we used the fluorescence signal from the knockout to develop an automated pipeline to identify and quantify acrolein intensity (Otsu two-class threshold and normalizing by the area of the cell). There was nearly no measurable somatic 8-oxo-dG signal in PV^+ neurons in the *Msh2*$^{+/+}$ TRN. To enable statistical comparison, we therefore quantified the minimal background 8-oxo-dG levels within PV^+ neuronal somata in *Msh2*$^{+/+}$ tissue. These values served as the baseline against which we compared the true 8-oxo-dG signal measured in PV^+ neurons from Msh2$^{-/-}$ mice. We measured mean intensity using ImageJ's ROI module. For statistical analysis of image quantifications, a Student's two-tailed *t*-test was conducted in GraphPad Prism 9 and Matlab.

In-vivo electrophysiology

A total of 2 *Msh2*$^{+/+}$ and 2 *Msh2*$^{-/-}$ were used for in vivo recordings of the TRN and ACx. Mice were given an IP injection of ketamine (75 mg/kg) and medetomidine (0.5 mg/kg) in 0.9 % NaCl for anesthetized recordings. Anesthesia was supplemented during surgery and throughout the recordings as needed. Following anesthesia, mice were kept on a heating pad at 36–38 °C while placed in a stereotaxic instrument containing head-fixed orbital bars, and a bite bar. To target the thalamic reticular nucleus, we made a craniotomy (approx. 3x2 mm^2) and durotomy centered at 2.07 mm lateral to the midline, and 1.3 mm posterior to bregma. A 32-channel silicone probe (Cambridge Neurotech) was lowered at a 15° angle relative to the midline, at a depth of 3.2–3.5 mm. The probe's recording sites spanned 775 μm. The exposed cortex was kept moist with cortex buffer ((in mM) 125 NaCl, 5 KCl, 10 Glucose, 10 HEPES, 2 $CaCl_2$, 2 $MgSO_4$) throughout the recording session. To target the auditory cortex, we made a craniotomy (approx. 3x2 mm^2) and durotomy centered at 1.5 mm anterior and 4 mm lateral to lambda. The exposed cortex was kept moist with cortex buffer. The probe was inserted into the auditory cortex at a depth of 800 μm ± 100 μm from the tip of the probe. The probe's recording sites spanned all layers of the cortex.

Recordings were obtained using Cheetah software (Neuralynx), with all data sampled at 31 kHz. All recordings were done in a sound-attenuated chamber, using a custom-built real-time Linux system (200 kHz sampling rate) driving a Lynx-22 audio card (Lynx Studio Technology, Newport Beach, California, USA) with an ED1 electrostatic speaker (Tucker-Davis Technologies, Alachua, Florida, USA) in a free-field configuration (speaker located 6 in. lateral to, and facing the contralateral ear). Recordings from the thalamic reticular nucleus were done in the absence of stimuli to assess spontaneous activity. Cortical recordings were stimulus driven. The stimuli were created with custom MATLAB scripts to compute tuning curves. We used a stimulus set that contained: a suite of pure tones (16 frequencies, 3 amplitudes: 20, 50, 80 dB) that lasted 100 ms.

In-vivo analysis

For analysis of in vivo recordings, we used Kilosort and Phy to sort spikes, extract spike times, and determine spike clusters. Spike clusters were determined to be in the TRN based on their position along the probe relative to the depth that the probe was lowered to. Only narrow spiking neurons were included in the analyses. Following spike sorting and clustering, we used custom MATLAB scripts to analyze spiking activity, as well as tone responses for cortical recordings. To determine the variability of spike trains in TRN neurons, we calculated the coefficient of variation of inter-spike intervals (ISIs), formally known as the Cv2 metric. The calculation for Cv2 was first described in Holt et al (Holt et al., 1996), and is as follows: $(2 \times |\Delta t_{(n+1)} - \Delta t_n|)/|\Delta t_{(n+1)} + \Delta t_n|$, where Δt_n describes the ISI. To analyze cortical recordings, we computed tuning curves for all clusters. After computing tuning curves, we determined their onset firing rate by counting the number of spikes within a 100 ms period after the start of the stimulus. We calculated tone responsive fields (TRFs) to the tones using these firing rates. Intensity thresholds were then determined by measuring the lowest intensity at which each cluster responded with a time-locked response in 25 % of the trials presented at that intensity (as previously described in South and Weinberger, 1995). Bandwidths were also determined for each cluster at 50 dB and 80 dB by using the lowest and highest frequency at which the clusters responded in 25 % of the trials presented. In general, we observed fewer tone responsive clusters of neurons in *Msh2*$^{-/-}$ compared to *Msh2*$^{+/+}$ across the same number of recording sites. Therefore, for all analyses we randomly sampled clusters from *Msh2*$^{+/+}$ mice to match the same number of clusters analyzed in *Msh2*$^{-/-}$ animals. For these analyses, cluster outliers were removed after matching the number of clusters across genotypes. For statistical analysis a Student's two-tailed *t*-test was conducted in GraphPad Prism 9 and Matlab.

Data availability

All the data values utilized for statistical comparisons, along with their corresponding statistics, are included in the Source Data file. The raw data from this study are available upon request from the corresponding author (H. V. Oviedo), due to the dataset's size.

Code availability

The code used to analyze spiking data is available in the Source Data of this paper.

CRediT authorship contribution statement

Sadia N. Rahman: Writing – review & editing, Writing – original draft, Investigation, Formal analysis, Data curation, Conceptualization. **Demetrios Neophytou:** Formal analysis, Data curation. **Siboney Oviedo-Gray:** Formal analysis, Data curation. **Bao Q. Vuong:** Supervision, Resources, Project administration, Funding acquisition, Conceptualization. **Hysell V. Oviedo:** Supervision, Resources, Project administration, Conceptualization, Writing – review & editing, Formal analysis, Data curation.

Declaration of Competing Interest

The authors declare that they have no known competing financial interests or personal relationships that could have appeared to influence the work reported in this paper.

Acknowledgements

We would like to thank Emily Sible, Mark Emerson and Pinar Ayata for valuable feedback on the project; Laura Nicolas-Gomariz for feedback on the manuscript; Michael Barkasi for cross-correlation analysis. We would like to thank Gabriel Gray for troubleshooting the acrolein immunohistochemistry. This work was funded by a National Cancer Institute grant U54CA132378 to B.Q.V. and a National Institute of General Medical Sciences grant SC1GM132035 to B.Q.V.

Author contributions

S.N.R. performed and analyzed the c-Fos, PV, and connexin immunohistochemistry; D.N. performed and analyzed the in vivo electrophysiology experiments, S.O.G. performed and analyzed the acrolein immunohistochemistry; H.V.O. stimulated, perfused animals, and performed 8-oxo-dG immunohistochemistry. S.N.R., H.V.O., and B.Q.V. drafted and edited the manuscript; B.Q.V. and H.V.O. coordinated the study.

Appendix A. Supplementary data

Supplementary data to this article can be found online at https://doi.org/10.1016/j.neuroscience.2025.12.066.

References

Hoeijmakers, J.H., 2009. DNA damage, aging, and cancer. N. Engl. J. Med. 361, 1475–1485. https://doi.org/10.1056/NEJMra0804615.

McKinnon, P.J., 2009. DNA repair deficiency and neurological disease. Nat. Rev. Neurosci. 10, 100–112. https://doi.org/10.1038/nrn2559.

Orii, K.E., Lee, Y., Kondo, N., McKinnon, P.J., 2006. Selective utilization of nonhomologous end-joining and homologous recombination DNA repair pathways during nervous system development. PNAS 103, 10017–10022. https://doi.org/10.1073/pnas.0602436103.

Liu, D., Keijzers, G., Rasmussen, L.J., 2017. DNA mismatch repair and its many roles in eukaryotic cells. Mutat. Res. Rev. Mutat. Res. 773, 174–187. https://doi.org/10.1016/j.mrrev.2017.07.001.

Jiricny, J., 2006. The multifaceted mismatch-repair system. Nat. Rev. Mol. Cell Biol. 7, 335–346. https://doi.org/10.1038/nrm1907.

Tamura, K., et al., 2019. Genetic and genomic basis of the mismatch repair system involved in Lynch syndrome. Int. J. Clin. Oncol. 24, 999–1011. https://doi.org/10.1007/s10147-019-01494-y.

Baas, A.F., et al., 2013. Agenesis of the corpus callosum and gray matter heterotopia in three patients with constitutional mismatch repair deficiency syndrome. Eur. J. Hum. Genet. 21, 55–61. https://doi.org/10.1038/ejhg.2012.117.

Aronson, M., et al., 2022. Diagnostic criteria for constitutional mismatch repair deficiency (CMMRD): recommendations from the international consensus working group. J. Med. Genet. 59, 318–327. https://doi.org/10.1136/jmedgenet-2020-107627.

Russo, M.T., et al., 2009. Role of MUTYH and MSH2 in the control of oxidative DNA damage, genetic instability, and tumorigenesis. Cancer Res. 69, 4372–4379. https://doi.org/10.1158/0008-5472.CAN-08-3292.

Iyer, R.R., Pluciennik, A., Napierala, M., Wells, R.D., 2015. DNA triplet repeat expansion and mismatch repair. Annu. Rev. Biochem 84, 199–226. https://doi.org/10.1146/annurev-biochem-060614-034010.

Kovalenko, M., et al., 2012. Msh2 acts in medium-spiny striatal neurons as an enhancer of CAG instability and mutant huntingtin phenotypes in Huntington's disease knock-in mice. PLoS One 7, e44273. https://doi.org/10.1371/journal.pone.0044273.

Schmidt, M.H.M., Pearson, C.E., 2016. Disease-associated repeat instability and mismatch repair. DNA Repair (Amst) 38, 117–126. https://doi.org/10.1016/j.dnarep.2015.11.008.

Fishel, M.L., Vasko, M.R., Kelley, M.R., 2007. DNA repair in neurons: so if they don't divide what's to repair? Mutat. Res. 614, 24–36. https://doi.org/10.1016/j.mrfmmm.2006.06.007.

Iyama, T., Wilson 3rd., D.M., 2013. DNA repair mechanisms in dividing and non-dividing cells. DNA Repair (Amst) 12, 620–636. https://doi.org/10.1016/j.dnarep.2013.04.015.

Science, A. I. f. B. Msh2 - RP_060220_02_F12 - coronal. Experiment detail. *Allen Brain Atlas: Mouse brain*, doi:https://mouse.brain-map.org/experiment/show/74657951.

Ramskold, D., Wang, E.T., Burge, C.B., Sandberg, R., 2009. An abundance of ubiquitously expressed genes revealed by tissue transcriptome sequence data. PLoS Comput. Biol. 5, e1000598. https://doi.org/10.1371/journal.pcbi.1000598.

Diouf, B., et al., 2016. Msh2 deficiency leads to dysmyelination of the corpus callosum, impaired locomotion, and altered sensory function in mice. Sci. Rep. 6, 30757. https://doi.org/10.1038/srep30757.

Robertson, C.E., et al., 2014. Global motion perception deficits in autism are reflected as early as primary visual cortex. Brain 137, 2588–2599. https://doi.org/10.1093/brain/awu189.

de Wind, N., Dekker, M., Berns, A., Radman, M., te Riele, H., 1995. Inactivation of the mouse Msh2 gene results in mismatch repair deficiency, methylation tolerance, hyperrecombination, and predisposition to cancer. Cell 82, 321–330. https://doi.org/10.1016/0092-8674(95)90319-4.

Levy, R.B., et al., 2019. Circuit asymmetries underlie functional lateralization in the mouse auditory cortex. Nat. Commun. 10, 2783. https://doi.org/10.1038/s41467-019-10690-3.

Peruzzi, D., Bartlett, E., Smith, P.H., Oliver, D.L., 1997. A monosynaptic GABAergic input from the inferior colliculus to the medial geniculate body in rat. J. Neurosci. 17, 3766–3777. https://doi.org/10.1523/JNEUROSCI.17-10-03766.1997.

Coombes, S., Zachariou, M., 2009. Gap junctions and Emergent Rhythms. Springer Series in Computational Neuroscience 3, 77–94.

Crabtree, J.W., 2018. Functional Diversity of Thalamic Reticular Subnetworks. Front. Syst. Neurosci. 12, 41. https://doi.org/10.3389/fnsys.2018.00041.

Alberi, L., Lintas, A., Kretz, R., Schwaller, B., Villa, A.E., 2013. The calcium-binding protein parvalbumin modulates the firing 1 properties of the reticular thalamic nucleus bursting neurons. J. Neurophysiol. 109, 2827–2841. https://doi.org/10.1152/jn.00375.2012.

Ruden, J.B., Dugan, L.L., Konradi, C., 2021. Parvalbumin interneuron vulnerability and brain disorders. Neuropsychopharmacology 46, 279–287. https://doi.org/10.1038/s41386-020-0778-9.

Runyan, C.A., et al., 2010. Response features of parvalbumin-expressing interneurons suggest precise roles for subtypes of inhibition in visual cortex. Neuron 67, 847–857. https://doi.org/10.1016/j.neuron.2010.08.006.

Landisman, C.E., et al., 2002. Electrical synapses in the thalamic reticular nucleus. J. Neurosci. 22, 1002–1009. https://doi.org/10.1523/JNEUROSCI.22-03-01002.2002.

Saez, J.C., Berthoud, V.M., Branes, M.C., Martinez, A.D., Beyer, E.C., 2003. Plasma membrane channels formed by connexins: their regulation and functions. Physiol. Rev. 83, 1359–1400. https://doi.org/10.1152/physrev.00007.2003.

Hartings, J.A., Temereanca, S., Simons, D.J., 2003. State-dependent processing of sensory stimuli by thalamic reticular neurons. J. Neurosci. 23, 5264–5271. https://doi.org/10.1523/JNEUROSCI.23-12-05264.2003.

Mendoza, A. J. & Haas, J. S. Intrinsic Sources and Functional Impacts of Asymmetry at Electrical Synapses. *eNeuro* **9**, doi:10.1523/ENEURO.0469-21.2022 (2022).

Steriade, M., Domich, L., Oakson, G., Deschenes, M., 1987. The deafferented reticular thalamic nucleus generates spindle rhythmicity. J. Neurophysiol. 57, 260–273. https://doi.org/10.1152/jn.1987.57.1.260.

Pinault, D., 2004. The thalamic reticular nucleus: structure, function and concept. Brain Res. Brain Res. Rev. 46, 1–31. https://doi.org/10.1016/j.brainresrev.2004.04.008.

Bartho, P., et al., 2014. Ongoing network state controls the length of sleep spindles via inhibitory activity. Neuron 82, 1367–1379. https://doi.org/10.1016/j.neuron.2014.04.046.

McAlonan, K., Cavanaugh, J., Wurtz, R.H., 2006. Attentional modulation of thalamic reticular neurons. J. Neurosci. 26, 4444–4450. https://doi.org/10.1523/JNEUROSCI.5602-05.2006.

Okuno, Y., Nakamura-Ishizu, A., Otsu, K., Suda, T., Kubota, Y., 2012. Pathological neoangiogenesis depends on oxidative stress regulation by ATM. Nat. Med. 18, 1208–1216. https://doi.org/10.1038/nm.2846.

Colussi, C., et al., 2002. The mammalian mismatch repair pathway removes DNA 8-oxodGMP incorporated from the oxidized dNTP pool. Curr. Biol. 12, 912–918. https://doi.org/10.1016/s0960-9822(02)00863-1.

Martin, S.A., et al., 2010. DNA polymerases as potential therapeutic targets for cancers deficient in the DNA mismatch repair proteins MSH2 or MLH1. Cancer Cell 17, 235–248. https://doi.org/10.1016/j.ccr.2009.12.046.

Wetzel, W., Ohl, F.W., Scheich, H., 2008. Global versus local processing of frequency-modulated tones in gerbils: an animal model of lateralized auditory cortex functions. PNAS 105, 6753–6758. https://doi.org/10.1073/pnas.0707844105.

Wetzel, W., Ohl, F.W., Wagner, T., Scheich, H., 1998. Right auditory cortex lesion in Mongolian gerbils impairs discrimination of rising and falling frequency-modulated tones. Neurosci. Lett. 252, 115–118. https://doi.org/10.1016/s0304-3940(98)00561-8.

Li, Y., et al., 2020. Distinct subnetworks of the thalamic reticular nucleus. Nature 583, 819–824. https://doi.org/10.1038/s41586-020-2504-5.

Cernotova, D., Hruzova, K., Levcik, D., Svoboda, J., Stuchlik, A., 2023. Linking Social Cognition, Parvalbumin Interneurons, and Oxytocin in Alzheimer's Disease: an Update. J. Alzheimers Dis. 96, 861–875. https://doi.org/10.3233/JAD-230333.

Filice, F., Vorckel, K.J., Sungur, A.O., Wohr, M., Schwaller, B., 2016. Reduction in parvalbumin expression not loss of the parvalbumin-expressing GABA interneuron subpopulation in genetic parvalbumin and shank mouse models of autism. Mol. Brain 9, 10. https://doi.org/10.1186/s13041-016-0192-8.

Wohr, M., et al., 2015. Lack of parvalbumin in mice leads to behavioral deficits relevant to all human autism core symptoms and related neural morphofunctional abnormalities. Transl. Psychiatry 5, e525.

Godoy, L.D., Prizon, T., Rossignoli, M.T., Leite, J.P., Liberato, J.L., 2022. Parvalbumin Role in Epilepsy and Psychiatric Comorbidities: from Mechanism to intervention. Front. Integr. Neurosci. 16, 765324. https://doi.org/10.3389/fnint.2022.765324.

Schwaller, B., et al., 2004. Parvalbumin deficiency affects network properties resulting in increased susceptibility to epileptic seizures. Mol. Cell. Neurosci. 25, 650–663. https://doi.org/10.1016/j.mcn.2003.12.006.

Nahar, L., Delacroix, B.M., Nam, H.W., 2021. The Role of Parvalbumin Interneurons in Neurotransmitter Balance and Neurological Disease. Front. Psych. 12, 679960. https://doi.org/10.3389/fpsyt.2021.679960.

Marlinski, V., Beloozerova, I.N., 2014. Burst firing of neurons in the thalamic reticular nucleus during locomotion. J. Neurophysiol. 112, 181–192. https://doi.org/10.1152/jn.00366.2013.

Caillard, O., et al., 2000. Role of the calcium-binding protein parvalbumin in short-term synaptic plasticity. PNAS 97, 13372–13377. https://doi.org/10.1073/pnas.230362997.

Crowe, S.L., Movsesyan, V.A., Jorgensen, T.J., Kondratyev, A., 2006. Rapid phosphorylation of histone H2A.X following ionotropic glutamate receptor activation. Eur. J. Neurosci. 23, 2351–2361. https://doi.org/10.1111/j.1460-9568.2006.04768.x.

Wang, H.Y., Lin, Y.P., Mitchell, C.K., Ram, S., O'Brien, J., 2015. Two-color fluorescent analysis of connexin 36 turnover: relationship to functional plasticity. J. Cell Sci. 128, 3888–3897. https://doi.org/10.1242/jcs.162586.

Roh, D.S., Funderburgh, J.L., 2011. Rapid changes in connexin-43 in response to genotoxic stress stabilize cell-cell communication in corneal endothelium. Invest. Ophthalmol. Vis. Sci. 52, 5174–5182. https://doi.org/10.1167/iovs.11-7272.

Hunter, A.W., Gourdie, R.G., 2008. The second PDZ domain of zonula occludens-1 is dispensable for targeting to connexin 43 gap junctions. Cell Commun. Adhes. 15, 55–63. https://doi.org/10.1080/15419060802014370.

Li, X., et al., 2004. Neuronal connexin36 association with zonula occludens-1 protein (ZO-1) in mouse brain and interaction with the first PDZ domain of ZO-1. Eur. J. Neurosci. 19, 2132–2146. https://doi.org/10.1111/j.0953-816X.2004.03283.x.

Shin, S., Walker, K. A. & Yoon, S. O. The PIKK-AKT connection in the DNA damage response. *Sci. Signal* **15**, eabm6211, doi:10.1126/scisignal.abm6211 (2022).

Pogoda, K., Kameritsch, P., Retamal, M.A., Vega, J.L., 2016. Regulation of gap junction channels and hemichannels by phosphorylation and redox changes: a revision. BMC Cell Biol. 17 Suppl 1, 11. https://doi.org/10.1186/s12860-016-0099-3.

Dudek, H., et al., 1997. Regulation of neuronal survival by the serine-threonine protein kinase Akt. Science 275, 661–665. https://doi.org/10.1126/science.275.5300.661.

Wong, F.K., et al., 2018. Pyramidal cell regulation of interneuron survival sculpts cortical networks. Nature 557, 668–673. https://doi.org/10.1038/s41586-018-0139-6.

Perez-Velazquez, J.L., Valiante, T.A., Carlen, P.L., 1994. Modulation of gap junctional mechanisms during calcium-free induced field burst activity: a possible role for electrotonic coupling in epileptogenesis. J. Neurosci. 14, 4308–4317. https://doi.org/10.1523/JNEUROSCI.14-07-04308.1994.

Zhang, Y., et al., 1998. Slow oscillations (</=1 Hz) mediated by GABAergic interneuronal networks in rat hippocampus. J. Neurosci. 18, 9256–9268. https://doi.org/10.1523/JNEUROSCI.18-22-09256.1998.

Skinner, F.K., Zhang, L., Velazquez, J.L., Carlen, P.L., 1999. Bursting in inhibitory interneuronal networks: a role for gap-junctional coupling. J. Neurophysiol. 81, 1274–1283. https://doi.org/10.1152/jn.1999.81.3.1274.

Lee, E., et al., 2021. Excitatory synapses and gap junctions cooperate to improve Pv neuronal burst firing and cortical social cognition in Shank2-mutant mice. Nat. Commun. 12, 5116. https://doi.org/10.1038/s41467-021-25356-2.

Shosaku, A., Sumitomo, I., 1983. Auditory neurons in the rat thalamic reticular nucleus. Exp. Brain Res. 49, 432–442. https://doi.org/10.1007/BF00238784.

Svirskis, G., Rinzel, J., 2000. Influence of temporal correlation of synaptic input on the rate and variability of firing in neurons. Biophys. J . 79, 629–637. https://doi.org/10.1016/S0006-3495(00)76321-1.

Li, J., et al., 2024. The Thalamocortical Mechanism underlying the Generation and Regulation of the Auditory Steady-State responses in Awake mice. J. Neurosci. 44. https://doi.org/10.1523/JNEUROSCI.1166-23.2023.

Roussel, C., Erneux, T., Schiffmann, S.N., Gall, D., 2006. Modulation of neuronal excitability by intracellular calcium buffering: from spiking to bursting. Cell Calcium 39, 455–466. https://doi.org/10.1016/j.ceca.2006.01.004.

Bischop, D.P., Orduz, D., Lambot, L., Schiffmann, S.N., Gall, D., 2012. Control of neuronal excitability by calcium binding proteins: a new mathematical model for striatal fast-spiking interneurons. Front. Mol. Neurosci. 5, 78. https://doi.org/10.3389/fnmol.2012.00078.

Rungta, R.L., et al., 2015. The cellular mechanisms of neuronal swelling underlying cytotoxic edema. Cell 161, 610–621. https://doi.org/10.1016/j.cell.2015.03.029.

Kang, M.A., So, E.Y., Simons, A.L., Spitz, D.R., Ouchi, T., 2012. DNA damage induces reactive oxygen species generation through the H2AX-Nox1/Rac1 pathway. Cell Death Dis. 3, e249.

Juan, C. A., Perez de la Lastra, J. M., Plou, F. J. & Perez-Lebena, E. The Chemistry of Reactive Oxygen Species (ROS) Revisited: Outlining Their Role in Biological Macromolecules (DNA, Lipids and Proteins) and Induced Pathologies. Int. J. Mol. Sci. **22**, doi:10.3390/ijms22094642 (2021).

Zhang, L., et al., 2024. Role of NLRP3 inflammasome in central nervous system diseases. Cell Biosci. 14, 75. https://doi.org/10.1186/s13578-024-01256-y.

Anderson, F.L., Biggs, K.E., Rankin, B.E., Havrda, M.C., 2023. NLRP3 inflammasome in neurodegenerative disease. Transl. Res. 252, 21–33. https://doi.org/10.1016/j.trsl.2022.08.006.

Huguenard, J.R., Prince, D.A., 1992. A novel T-type current underlies prolonged Ca(2+)-dependent burst firing in GABAergic neurons of rat thalamic reticular nucleus. J. Neurosci. 12, 3804–3817. https://doi.org/10.1523/JNEUROSCI.12-10-03804.1992.

Holt, G.R., Softky, W.R., Koch, C., Douglas, R.J., 1996. Comparison of discharge variability in vitro and in vivo in cat visual cortex neurons. J. Neurophysiol. 75, 1806–1814. https://doi.org/10.1152/jn.1996.75.5.1806.

South, D.A., Weinberger, N.M., 1995. A comparison of tone-evoked response properties of 'cluster' recordings and their constituent single cells in the auditory cortex. Brain Res. 704, 275–288. https://doi.org/10.1016/0006-8993(95)01134-x.